

JGR Solid Earth

RESEARCH ARTICLE

10.1029/2024JB030625

Key Points:

- Spatial distribution of uplift across the Southern Alps is measured using Sentinel-1 InSAR
- Heightened uplift around Aoraki/Mt Cook due to the shallowing of the Alpine Fault, which is shown to be capable of hosting $M_w > 8$ earthquakes
- Variations in exhumation rates may be inferred from modern geodetic observations if a mountain range has attained steady state

Supporting Information:

Supporting Information may be found in the online version of this article.

Correspondence to:

J. D. McGrath,
jack.mcgrath@canterbury.ac.nz

Citation:

McGrath, J. D., Elliott, J. R., Watson, A. R., Wright, T. J., Piazzolo, S., & Hamling, I. J. (2025). Linking geodetically resolved uplift to long-term orogenic exhumation in the Southern Alps, New Zealand. *Journal of Geophysical Research: Solid Earth*, 130, e2024JB030625. <https://doi.org/10.1029/2024JB030625>

Received 24 OCT 2024

Accepted 22 OCT 2025

Author Contributions:

Conceptualization: Jack D. McGrath, John R. Elliott, Tim J. Wright, Sandra Piazzolo, Ian J. Hamling

Formal analysis: Jack D. McGrath, John R. Elliott

Funding acquisition: John R. Elliott, Tim J. Wright, Sandra Piazzolo, Ian J. Hamling

Investigation: Jack D. McGrath, John R. Elliott

Methodology: Jack D. McGrath, John R. Elliott, Andrew R. Watson, Tim J. Wright

Project administration: John R. Elliott

Resources: John R. Elliott

Software: Jack D. McGrath






Supervision: John R. Elliott, Tim

J. Wright, Sandra Piazzolo, Ian J. Hamling

© 2025. The Author(s).

This is an open access article under the terms of the [Creative Commons Attribution License](#), which permits use, distribution and reproduction in any medium, provided the original work is properly cited.

Linking Geodetically Resolved Uplift to Long-Term Orogenic Exhumation in the Southern Alps, New Zealand

Jack D. McGrath^{1,2} , John R. Elliott¹ , Andrew R. Watson³, Tim J. Wright^{1,3} , Sandra Piazzolo¹ , and Ian J. Hamling⁴ 

¹COMET, University of Leeds, Leeds, UK, ²Now at University of Canterbury, Christchurch, New Zealand, ³SatSense Ltd, Leeds, UK, ⁴GNS Science, Lower Hutt, New Zealand

Abstract A limitation in our understanding of the geodynamics of orogenies is the difficulty in resolving the spatial variations in long-term processes such as exhumation of the crust. Although geodesy can record ground motions to millimeter-scale precision at high spatial and temporal resolutions, these observations only cover a small fraction of the seismic cycle, and therefore may not represent the long-term behavior of an orogeny. Here, by considering various contributions to uplift over differing timescales, we attempt to constrain spatially resolved exhumation rates using observations of permanent interseismic uplift from InSAR, GPS, fault trenching and a range of modeling techniques. We apply our methodology to New Zealand's Southern Alps, an orogeny with known high exhumation rates and variable behavior along orogenic strike. We generate InSAR derived velocity fields which show uplift rates of up to 1 cm/yr focused around Aoraki/Mt Cook. Velocity field inversion shows that the structural make-up of the plate boundary exerts a major control on this spatial variability of exhumation due to a 15° shallowing of the Alpine Fault. Modeling the accumulated slip deficit indicates the Alpine Fault is capable of hosting great ($M_w > 8$) earthquakes. By combining the interseismic velocity fields and coseismic displacement rates, we produce a map of the exhumation rates in the Southern Alps. These observations indicate a tectonic cause for a connection between long-term uplift and exhumation in this region. With careful consideration of other uplift contributions, our approach may be used in other orogenic belts.

Plain Language Summary Establishing the connection between measurements of current ground motion and the long-term processes that control mountain growth is challenging due to the difference in timespans between the observations and tectonic processes. Current ground motion measurements often miss important events such as earthquakes that cumulatively contribute to the evolution of mountains. Using satellite images, we can create high spatial resolution maps of current ground motion over the Southern Alps, New Zealand. We show that the mountains there are growing by up to 1 cm a year in the past decade. This region of uplift is focused in the area around the highest peak, Aoraki/Mt Cook. By modeling the spatial pattern of uplift, we show that the structure and current slip rates of the major Alpine Fault change along strike. We confirm that enough strain has accumulated that an earthquake as big as magnitude 8 could happen on the Alpine Fault, and we calculate the amount of uplift that would occur coseismically because of such an event. Combining the estimated coseismic uplift and current uplift maps we measure today allows us to recreate the long-term growth pattern of the Southern Alps, which we confirm by comparing to other studies of exhumation.

1. Introduction

Although the measurement of contemporary orogenic uplift is conceptually simple, unraveling how this reflects the long-term exhumation behavior of orogenies is challenging. The tectonic control of uplift and the interplay of geological processes play a critical role in shaping orogenies over geological timescales. Earthquakes can induce rapid changes in elevation, as seen in events like Wenchuan (Parker et al., 2011) and the Gorkha earthquakes (Elliott et al., 2016; Hubbard et al., 2016), but if these changes lack tectonic support, isostatic compensation leads to recovery that may largely reverse them (Molnar, 2012). Additionally, climatically driven processes such as glaciation, precipitation and erosion has the ability to enable both the growth of individual peaks (Han et al., 2024) and the overall configuration of orogenic systems (Molnar, 2012; Willett, 1999), although whether it provides the initial impetus to orogenic growth can be unclear (Molnar & England, 1990). Regardless, the long-term geological evolution of orogenies profoundly impacts climate dynamics, influencing carbon fluxes globally (Hilton & West, 2020) and affecting regional climates, such as the Himalayan monsoon patterns (Tada

Visualization: Jack D. McGrath, John R. Elliott, Andrew R. Watson
Writing – original draft: Jack D. McGrath
Writing – review & editing: John R. Elliott, Andrew R. Watson, Tim J. Wright, Sandra Piazzolo, Ian J. Hamling

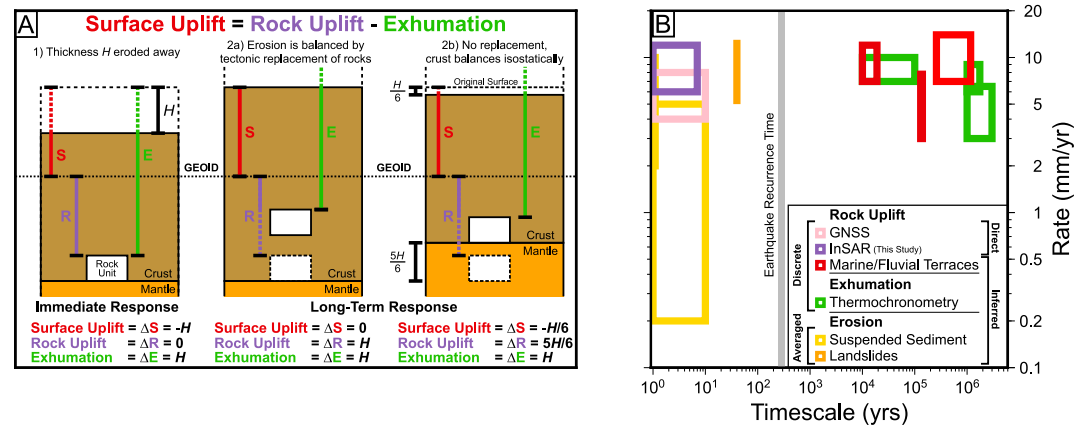


Figure 1. The relationship between exhumation, surface and rock uplift. (a) How uplift and exhumation relates to the amount erosion that has occurred depends as to whether the mass of eroded material is balanced by tectonic replacement of rocks. Mass balancing from the addition of material during crustal thickening results in long-term surface stability with no isostatic adjustment, where apparent surface uplift equals exhumation. Without mass balancing, crustal thinning causes an isostatic response and the recovery of $\sim 5/6$ of the surface change without the need for any additional tectonic process (Molnar & England, 1990). (b) Rock uplift, exhumation and erosion are consistent over multiple methods and timescales in the Southern Alps. Methods are distinguished between those that assign rates to discrete points or are averaged over catchment areas, or by methods that provide direct (i.e., geodetic) or inferred measurements. Adapted from (Jiao et al., 2017), including data from (Adams, 1981; Hovius et al., 1997). Box colors correspond to those in panel (a).

et al., 2016). The influence of climate, particularly through erosion and sediment transport, can further complicate this relationship. Notably, whilst much orogenic growth occurs through earthquakes on fault zones during continental collisions (Dal Zilio et al., 2021), the evolution of shear fabrics and tectonic structures indicates that much of this deformation occurs through ductile processes over extended periods (Little et al., 2005; Norris & Toy, 2014).

In understanding the behavior of orogens, we ideally want to get at rates and spatial patterns of exhumation, but the measurements we are able to make are more typically those of uplift. This study aims to examine the link between observations of contemporary surface uplift, and propose a methodology by which it may be related to the spatial distribution of exhumation. We use the Southern Alps and Alpine Fault, New Zealand as a case study. We start by examining the relationship between uplift and exhumation, and the contributions that various processes will provide. We then apply this thought process to the Southern Alps, where we first use Interferometric Synthetic Aperture Radar (InSAR) to generate velocity fields of the current interseismic ground motion. Inversion of these velocity fields will allow us to describe the current geometry, locking distribution, and slip-rate deficits of the Alpine Fault, the major transpressive plate margin upon which the Southern Alps has formed. By taking the resulting locking pattern and slip-rate deficit, we are able to model the uplift pattern associated with a rupture on the Alpine Fault. If the currently observed interseismic uplift rates represent the end member of anelastic deformation, by combining the interseismic uplift rates with the co-seismic uplift, this can represent rock uplift over the seismic cycle. If a negligible isostatic response can be assumed, due to a mass balance between crustal material underplating the Southern Alps and the amount of material removed via erosion, we suggest that the pattern of long-term rock uplift should be equal to that of exhumation. This is then compared to a published exhumation model to assess if it may be suitable as a first-order exhumation proxy.

2. The Relation Between Uplift and Exhumation

Current topography is produced as a result of the interplay between constructive and destructive orogenic processes, which England and Molnar (1990) represent as:

$$\text{Surface Uplift} = \text{Rock Uplift} - \text{Exhumation} \quad (1)$$

where surface and rock uplift are the vertical motion of the ground surface and rock units relative to a reference geoid, and exhumation is the change in vertical distance between a rock unit and the surface (Figure 1a). Whilst

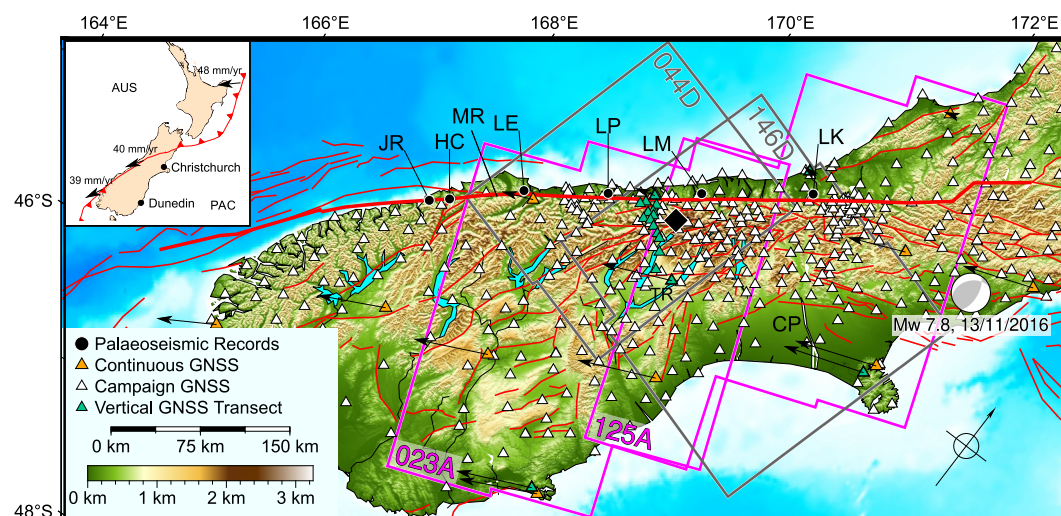


Figure 2. Overview of selected geophysical and palaeoseismic data collection in South Island. Palaeoseismic records from lakes and swamps described by Howarth et al. (2021) (HC: Hokuri Creek, JR: John O'Groats River, LE, LP, LM, and LK: Lakes Ellery, Paringa, Mapourika and Kaniere respectively). Horizontal GNSS stations were used for the NZ velocity field (Beavan et al., 2016), and verticals for the Karangarua transect (Beavan et al., 2010). Pink and gray polygons are ascending and descending Sentinel-1 footprints. Faults from the New Zealand Active Faults Database (Langridge et al., 2016). Aoraki/Mt Cook (3,726 m) indicated by the black diamond. MR: Martyr River, TR: Tekapo River, CP: Canterbury Plain. Inset: Plate boundary variation across New Zealand. Arrows are Pacific Plate motion.

this remains a notionally simple relationship, particularly over timescales of millions of years, complexity is introduced when considering the effects at variable timescales. For instance, over the course of an earthquake cycle, it becomes impractical to consider uplift as a single rate rather than as a long-term rate, which discrete, coseismic jumps act upon. As a further complication, the impact of seismic contributions becomes a function of distance from the fault as well as the length of time since the last earthquake. However, it is important to be able to unravel the various contributions in order to be able to correctly interpret what we observe today as a guide to understanding the dynamics and forces in the past that have created such mountains, and its associated contribution to seismic hazard.

To examine the relationship between contemporaneous uplift and longer-term exhumation measured over multiple time-scales, we use New Zealand's Southern Alps as a study area. The region hosts major earthquakes that contribute to its ongoing fault and orogenic evolution, and its rapid deformation should be detectable with InSAR over whole mountain scales, despite being a challenging target. The Southern Alps has formed due to oblique transpression of the Pacific-Australian plate boundary along the Alpine Fault (AF) (Figure 2: inset), creating a rapidly exhuming and deforming orogeny along a major fault with significant structural variations. Dextral slip on the Alpine Fault began in the early Miocene, with an increase in convergence rate at 6 Ma causing significant uplift and exhumation (Jiao et al., 2017; Sutherland, 1995). Approximately 40 mm/yr of relative Pacific Plate motion is accommodated along this boundary (Beavan et al., 2002), resulting in one of the fastest straining onshore regions on Earth (Haines & Wallace, 2020; Kreemer et al., 2014). ~30% of this plate motion is accommodated through internal deformation of the Southern Alps, with the remaining 70% (~27 mm/yr) occurring due to either interseismic or earthquake-induced slip on the Alpine Fault. Palaeoseismic trenching shows that the central Alpine Fault is capable of great ($M_w > 8$) earthquakes, last occurring in 1717, with a recurrence time of 249–329 years (Berryman et al., 2012; Howarth et al., 2021; Sutherland et al., 2007).

The addition of material to the Southern Alps by tectonically induced crustal thickening is balanced by mass removal due to erosional processes (Adams, 1980; Herman et al., 2010; Jiao et al., 2017; Molnar & England, 1990; Willett & Brandon, 2002), which otherwise would lead to 0.5–1.3 mm/yr of uplift due to isostatic compensation of Holocene erosion (Liu et al., 2024). Peak erosion, exhumation and uplift rates of 7–13 mm/yr are consistent across multiple time-scales (Figure 1b and Adams, 1980; Bull & Cooper, 1986; Herman et al., 2009, 2010; Hovius et al., 1997; Jiao et al., 2017; Little et al., 2005; Michailos et al., 2020; Simpson et al., 1994). This allows for a simplifying assumption to be made that the viscoelastic response of the mantle to the addition and

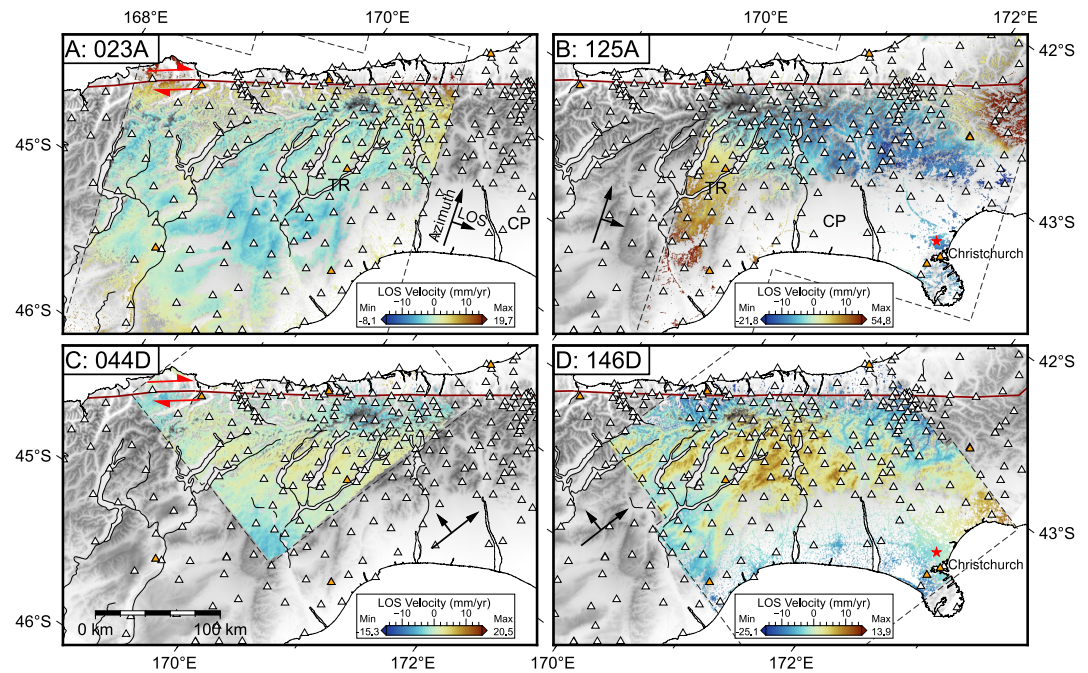


Figure 3. Line-of-Sight velocity fields for each S-1 track. (a–d), Line-of-Sight (LOS) velocity maps from each of the 4 Sentinel-1 frames outlined in Figure 2. Range increase is positive. For (b), 125A, the postseismic effects of the 2017 Kaikoura earthquake can be seen (high velocity region in the top right of the frame, focal mechanism shown in Figure 2), though the magnitude of these have spatially decayed by the overlap region. TR: Tekapo River, CP: Canterbury Plain.

removal of crustal material can be considered negligible, due to the long-term stability of the orogeny. However, there may be an additional quantifiable isostatic response due to ice unloading which can contribute to the observed vertical signal (Liu et al., 2024) which we also explore.

3. Impact of Timescale on Measurements of Uplift Rates

Although uplift rates are simplifiable to single values when averaged over long time periods (Equation 1), they can become increasingly variable over shorter timescales (especially within seismic cycles of hundreds of years). The short-term exhumation rates are a function of erosion rates, varying from not eroding at all, to gradual chemical or physical weathering, to landslides which instantly remove significant quantities of surface material. Tectonic rock uplift can be partitioned into seismic and aseismic (or coseismic and interseismic) components, with the relative contribution of each varying based on distance to the fault, and may be difficult to disentangle (Francis et al., 2020; Li et al., 2019). Over the timescale of multiple earthquake cycles, the total rock uplift comprises of the non-recoverable uplift contributions from interseismic deformation and coseismic displacement, and the resulting isostatic adjustments (Molnar, 2012). The elastic response of the crust following glacial retreat may also be considered within the isostatic term if it is significant enough to be observable (Liu et al., 2024). Although significant uplift can occur as a result of coseismic displacement, much of this deformation can be recovered elastically during afterslip (e.g., Wang et al., 2012; Weiss et al., 2019). The majority of the plastic strain accumulated in orogenies, however, accumulates because of the interseismic deformation (Baden et al., 2022).

Although coseismic rock uplift can be represented in the long term as a rate, in reality it is the summation of displacements occurring during the total number of earthquakes (n_{eq}), and so at any given point within a single earthquake cycle it may be close to 0, except for high displacements during an earthquake, and residual post-seismic displacements afterward. For orogens under long-term tectonic stability, where the mean topographic surface is preserved, long-term rock uplift and exhumation rates are equal.

Methods that can resolve long-term rock uplift and exhumation, such as uplifted marine terraces and thermochronometry, typically have coarse spatial resolution. Although the spatial variation in exhumation rate can be modeled by combining thermochronometry with higher-resolution data sets such as microseismic catalogs (cf.

Figure 5a and Jiao et al., 2017; Michailos et al., 2020), these approaches can be impractical and expensive to upscale.

However, routine observations of current surface motion can be made at orogenic and continental scales (e.g., Biggs & Wright, 2020; Crosetto et al., 2020; Hamling et al., 2022; Wright et al., 2023) following the advent of freely available data products from space-based geodetic techniques such as Global Navigation Satellite Systems (GNSS) and InSAR. Despite the high precision and spatial resolution of these measurements, they describe geologically short time periods (10^0 – 10^1 yr), and therefore may not be representative of deformation spanning complete seismic cycles (10^2 – 10^4 yr) or long-term orogenic exhumation and deformation (10^5 – 10^7 yr; Figure 2b).

Geodesy measures the net result of all uplift and subsidence within a given observation period. The degree of ambiguity as to how much of this motion at any given point is tectonic may be resolved by removing all transient non-tectonic signals from the data. Such inferences are estimates of contemporary rock uplift, as they should be unaffected by erosion, from either a lack of detectable surface level change due to the erosional processes being too slow (e.g., chemical weathering) to cause decorrelation, or so rapid (e.g., landsliding) that the uplift is immeasurable in GNSS or InSAR.

Assuming a region is sufficiently far into a seismic cycle that there is no longer any long-term earthquake contribution to uplift (such as after-slip and post-seismic relaxation) and the equilibrium state of the orogeny renders isostatic uplift negligible, then the measured interseismic uplift rate at the surface will be the tectonic contributions to surface uplift, and equal to the rock uplift rate. Therefore, if we take the end member scenario of all uplift due to interseismic deformation is non-recoverable, then as aseismic exhumation rates are constant for timescales >10 ka in areas where geodetic rates are steady during the earthquake cycle (Avouac, 2015), the tectonic contribution to surface uplift will equal the exhumation rate (Figure 1a). This allows us to use the tectonic surface uplift as an upper bound for exhumation in regions with no vertical component due to other factors such as coseismic displacement, isostatic adjustment, GIA, aquifers etc. The tectonic contribution to surface uplift will underestimate exhumation in coseismically affected regions, unless corrected for the near-fault uplift and far-field deformation by modeling the expected coseismic slip on the underlying fault structure (Elliott et al., 2016). Any uplifted material is then rapidly removed by processes such as seismically induced landsliding (Francis et al., 2020).

We therefore use a staged approach that allows recreation of spatial variations in exhumation rate from InSAR measurements of interseismic ground motion over a stable orogen. By inverting the interseismic motion to ascertain variations in fault structure and slip rate, and comparing to the measurements of the geological slip rate, the expected coseismic deformation can be modeled from the slip deficit. Summing the measured interseismic uplift rate with the modeled coseismic provides the distribution of bulk uplift for a seismic cycle, which can be used as an exhumation proxy. It should be noted that exhumation may also be the result of extensional tectonics resulting in a surface decrease (England & Molnar, 1990), but such regimes are outside the scope of this current study and are not considered further. We apply our suggested approach to the Southern Alps of New Zealand, a case study with spatial and temporal complexities.

4. Generating Velocity Fields From InSAR

The regional horizontal ground motion is well constrained by an extensive GNSS network, with regular campaigns allowing a national coverage on 8-year cycles (Beavan et al., 2016). However, the sparse distribution of continuous GNSS across South Island limits their use in measuring spatial patterns of vertical ground motion (Figure 2), with a dedicated vertical GNSS transect along the Karangarua Range (south of the peak uplift zone) recording peak uplift rates of 5 mm/yr (Figure 1b and Beavan et al., 2010). A national velocity field has been created utilizing both the horizontal velocities from the Vertical Derivatives of Horizontal Stress (Haines & Wallace, 2020) and ascending ENVISAT InSAR data from 2003 to 2011 (Hamling et al., 2022). However, the resulting vertical rates are inconsistent with the Karangarua transect. Therefore, to accurately capture vertical rates in mountainous areas, we take advantage of the large number of ascending and descending Sentinel-1 SAR acquisitions from the past decade.

We generate wrapped interferograms for the four overlapping Sentinel-1 (S-1) tracks (Figure 2) using the LiCSAR processing system (Lazecký et al., 2020). The region of interest is a challenging target for InSAR, with large areas incoherent for much of the winter months. Therefore, we select the interferogram network for each

track (Figure S1 in Supporting Information S1) based off a 90×30 km common area of interest parallel to the fault, using a coherence matrix to select interferograms that have a mean coherence in this area higher than 0.15 (Biggs et al., 2007). This method prioritizes interferograms that are coherent in the Pacific Plate, near to the Alpine Fault, at the expense of the low-lying, vegetated coastal regions, which are most coherent during the winter months. Therefore, by focusing only on high coherence interferograms by selecting image pairs coherent over the central Southern Alps, we generate networks of 170–1094 interferograms from 53 to 97 epochs (Figure S1 in Supporting Information S1) where short-baseline summer networks are joined by year or multi-year coherent interferograms.

This approach results in a large disparity between the number of interferograms used in the track 023A and the remaining tracks. However, given that velocity uncertainty is estimated by

$$\sigma_v = \frac{2\sqrt{3}\sigma_e}{N^{0.5}T} \quad (2)$$

where σ_e is the uncertainty of each epoch, N is the number of SAR acquisitions and T is the connected observation time period, the dominant control on velocity uncertainty is the time-span of the network, which is approximately equal across all three tracks (Morishita et al., 2020).

Interferograms are unwrapped and inverted for line-of-sight (LOS) velocities for each track using StaMPS (Hooper et al., 2012; Figures 3a–3d). To reduce unwrapping errors, we used the iterative unwrapping technique whilst removing a linear topographic Atmospheric Phase Screen (APS; Bekaert et al., 2015; Hussain, Hooper, et al., 2016). The LOS velocity for track 125A is particularly affected by noise, with significant contamination in the north due to post-seismic relaxation following the Kaikoura earthquake. Although both tracks 023A and 125A show a range decrease near to the fault, there is a seeming reversal in the LOS velocity in the southern section of the 125A frame (Figure 3b, lower-left). This is likely due to contamination of the data here due to unwrapping errors that were not corrected in the iterative unwrapping stage. A likely reason for this is incoherence in the Canterbury Plain and across the Tekapo River resulting in this region being isolated in many interferograms, of which there are relatively few in this region due to the focus on near-field coherence. These errors bleed into the vertical velocities later, and their impacts removed via referencing to the GNSS transect (Figure 4).

The resulting velocity fields were placed into an Australian fixed-plate reference system by removing a residual plane between the LOS velocity and the LOS-projected GNSS velocity (Hussain, Wright, et al., 2016; Weiss et al., 2020). We account for the relative insensitivity of the InSAR in approximately northward motion (Brouwer & Hanssen, 2021) by projecting the north component of the GNSS velocity field (Beavan et al., 2016) into the InSAR LOS, and then removing it from the LOS velocity. The resulting velocity fields are then inverted from LOS to east and vertical components (Figure 5 and Figure S2 in Supporting Information S1, Wright et al., 2004), with the north component coming from the GNSS.

Inspection of the resulting vertical velocities show a residual linear trend between topography and uplift rate, indicating that not all the effects of APS have been successfully removed, and some is manifest in the vertical motion during inversion (Figure 4a). It is necessary, therefore, to remove the linear relation between APS and topography. However, not all of the correlation between increased uplift rate and topography may be due to atmospheric effects—rather, the areas of higher topography may simply be due to a higher uplift rate (Stevens & Avouac, 2015). An overcorrection of the APS uplift-vs-topography trend may remove some of this signal. Therefore, we first look to identify any uplift versus topography trend within the vertical GNSS data of Beavan et al. (2010), as this would not be atmospherically induced, and remove this trend from our InSAR data (Figure 4b). We then solve for and remove the APS component, before adding back the trend (Figure 4c), thus reducing the uplift-vs-topographic trend in the data (Figures 4c and 4d).

There still remains an increase in the uplift rates in the south-east, due to the noise within track 125A bleeding into the uplift rates during the inversion (Figure 4f). The source of this noise is unclear, but may be due to the selection of interferograms based on near-fault coherence resulting in more far-field unwrapping errors in a relatively isolated far-field region. As uplift rates at these distances should be close to 0 mm/yr (Hamling et al., 2022; Houlié & Stern, 2017), we remove these by referencing and de-ramping the vertical rates to the vertical transect. This is done by looking for the difference between the vertical transect, and InSAR pixels within 2 km of each GNSS

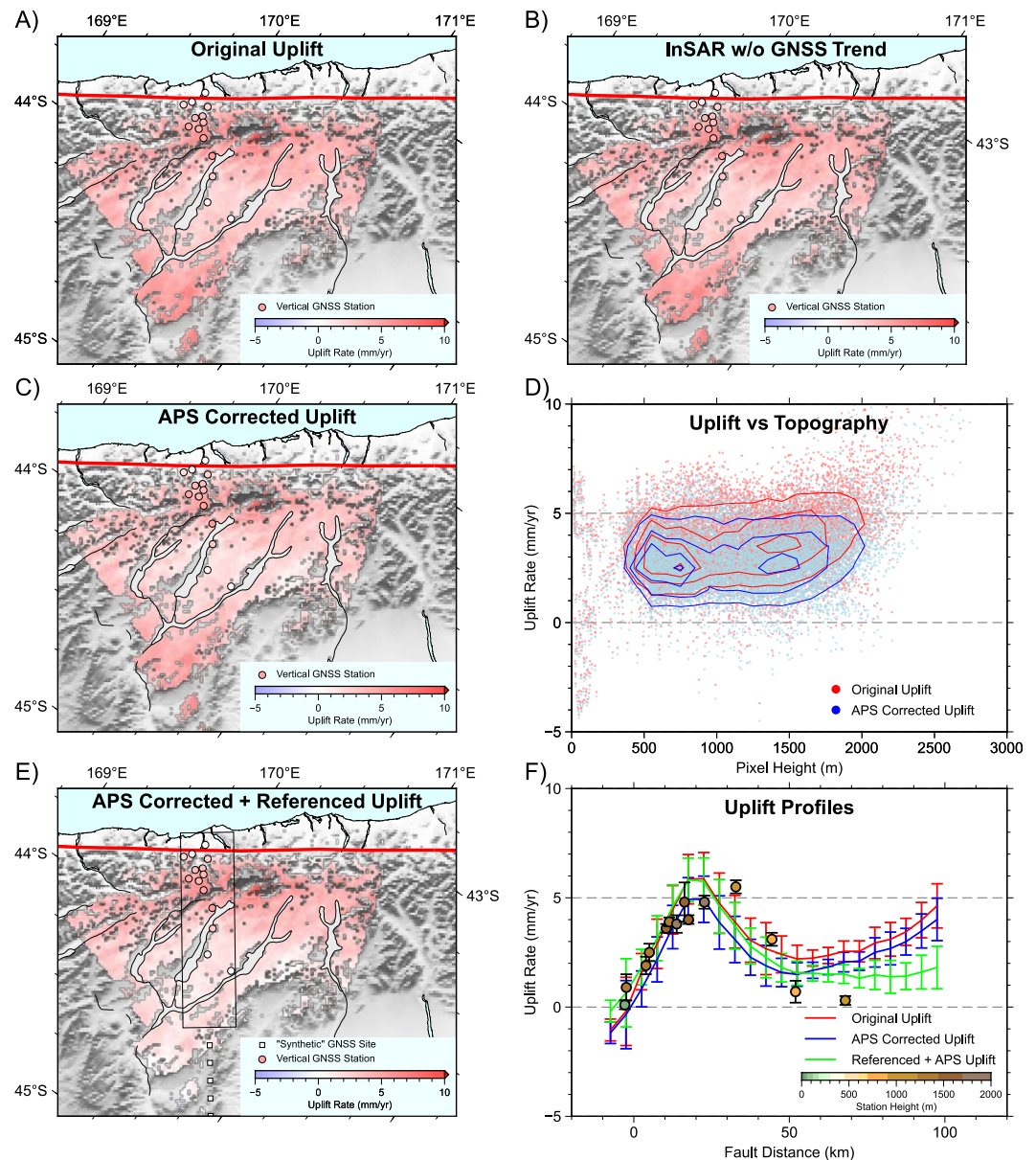


Figure 4. APS correction and referencing to GNSS of inverted uplift signal. (a) Original inverted uplift signal with vertical GNSS (Beavan et al., 2010). (b) Uplift after the linear relation between GNSS station elevation and GNSS uplift rate has been removed from all pixels. We consider this uplift to be due to tectonic processes, rather than atmospheric noise. (c) Uplift following removal of APS, and the returning of the GNSS uplift trend signal. (d) Reduction in uplift rate with topography before (Red) and after (Blue) APS removal. (e) Uplift following APS correction and referencing to GNSS transect. Black box shows profile used to plot results in panel (f). (f) Profiles along the swath highlighted in panel (c), showing the change in profile between the original (a, red), APS corrected (b, blue), and APS corrected and referenced InSAR uplift (c, green), and the GNSS uplift.

station, and fitting a second order polynomial to those residuals. As in the far field, where we expect no uplift, there are no vertical GNSS stations to fit the polynomial to, we pin the far field using 7 “synthetic” GNSS sites 110–170 km from the fault, with uplift rates set to 0 ± 1 mm/yr. By removing this polynomial trend from the InSAR, the far-field uptick in uplift is reduced, whilst preserving the good correlation between GNSS and uplift (Figures 4e and 4f).

Our measured uplift is focused in a region of 50×30 km around Aoraki/Mt Cook, a glaciated region around the maximum topography (3,724 m) in the Southern Alps, with uplift rates of 6–12 mm/yr (Figure 5a). Local

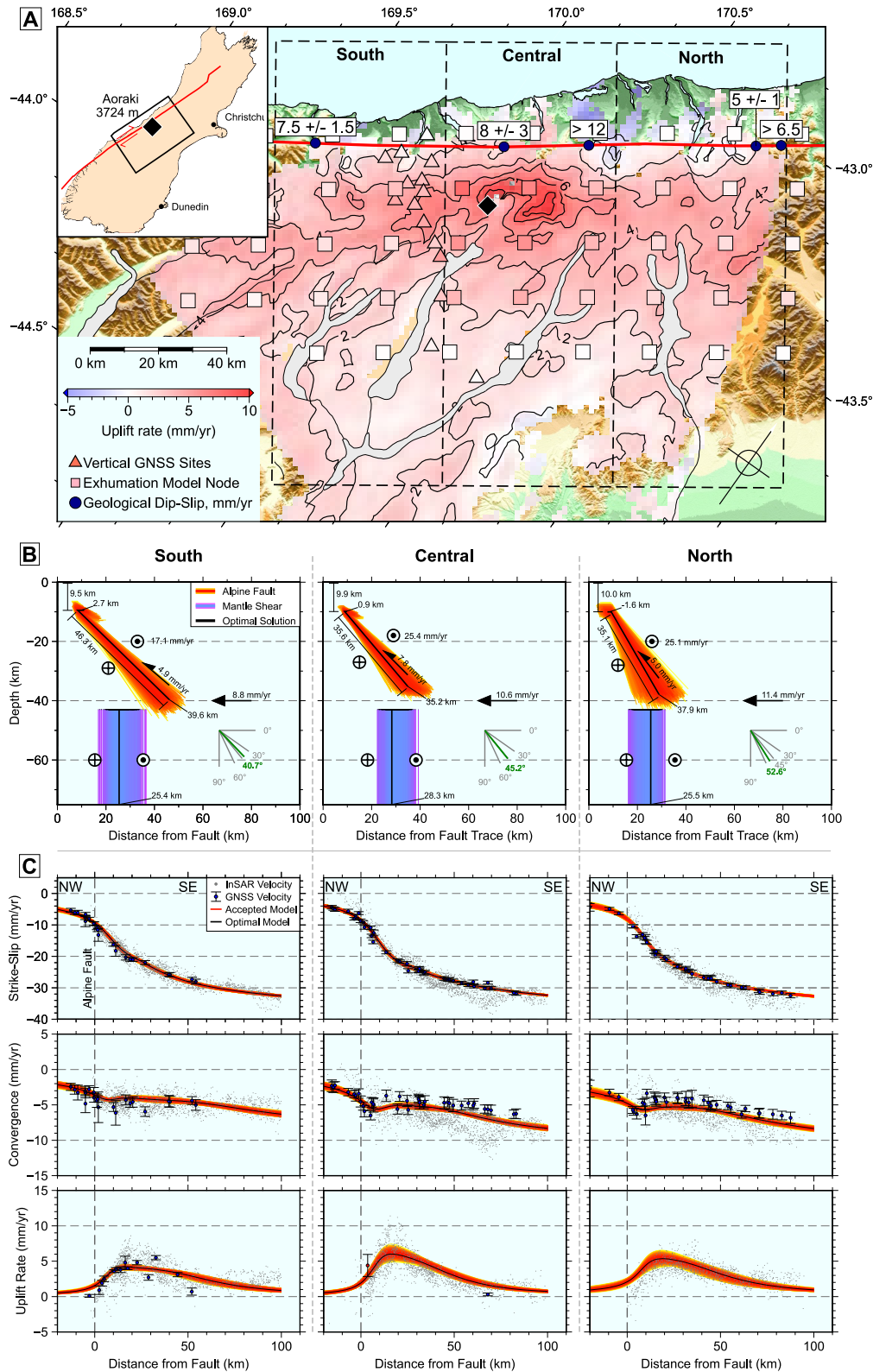


Figure 5.

reductions in the uplift rate within valleys and at the base of the glaciers are likely due to noise in the estimate of the uplift rate resulting from incomplete removal of pixels dominated by compaction of sediment load (Hamling et al., 2022). The numerous uplift, exhumation and erosion studies that have been carried out across the Southern Alps, using multiple techniques, provide several data sets against which to check the consistency of our InSAR derived uplift (Figure 1b). The use of more SAR acquisitions from multiple viewing geometries to create interferograms coherent over the central Southern Alps is likely why our uplift profiles are more consistent with GNSS than previous studies (Figure 5, Hamling et al., 2022).

5. The Impact of Glacial Isostatic Adjustment

We seek to quantify any additional isostatic response due to ice unloading which may contribute to the observed vertical signal, and examine how well it may be resolved by InSAR. This contribution can be separated into ice loss since the last glacial period, and modern ice loss since the end of the Little Ice Age (LIA) in 1600 (Carrivick et al., 2020).

Combined elastic and viscoelastic models indicate 0.3–0.5 mm/yr of isostatic uplift due to ice mass change during the last glacial period, remaining fairly constant along strike in the southern and central Southern Alps (Beavan et al., 2010; Liu et al., 2024; Schumacher et al., 2018). This remains below the detection limit of InSAR in this region, and would also have negligible impact of studies of along strike variations in fault properties.

Modern deglaciation since the Little Ice Age allows for larger, yet more localized GIA effects. We investigated the impact of modern deglaciation by differencing glacier ice surface measurements from the Little Ice Age (LIA) against glacier outlines for the year 1978, obtained from the Randolph Glacier Inventory (RGI), to come up with the spatial variation in the amount of ice lost (Carrivick et al., 2020), interpolated onto a 1 km grid. By taking 1600 as the end of the LIA, this ice loss can then be translated into a yearly ice loss rate, with the total ice loss rate across the Southern Alps of $-0.18 \text{ km}^3/\text{yr}$.

The highly localized variations in the vertical displacements (U_z) can then be calculated by considering the cumulative effect of the half-space Green's function for the point load of each grid cell, where:

$$U_z = \int \frac{g}{\pi} \times \frac{1-\nu^2}{E} \times \frac{m_{ice}}{r} \quad (3)$$

where g is gravitational acceleration, ν is Poisson's ratio (0.25), E is Young's Modulus of the crust ($6-9 \times 10^{10} \text{ Pa}$, Liu et al., 2024; Tesauero et al., 2013), m_{ice} is the amount of ice mass lost, and r is distance from the grid cell (Auriac et al., 2014; Boussinesq, 1878).

Taking these values results, the peak uplift rate is estimated to be 0.27–0.39 mm/yr at the Godley Glacier, and 0.23–0.34 mm/yr at the head of the Tasman Glacier (adjacent to Aoraki/Mt Cook), similar to the rates found by Beavan et al. (2010). A direct differencing of the LIA and RGI glacier lines can produce small areas of apparent thickening of the glacier. This would result in localized regions of subsidence, despite the expectations of glacial isostatic uplift due to ice loss. If this thickening is an artifact induced by differences in the processing steps used to generate the data sets, we also test an approach where we remove any potentially erroneous subsidence by filtering out any regions with apparent ice thickening. This increases peak uplift rates at both the Godley and Tasman glaciers of 0.30–0.44 mm/yr, with an overall peak of 0.35–0.51 mm/yr. As the ice loss rate in the Southern Alps has more than doubled to $-0.39 \text{ km}^3/\text{yr}$, doubling the ice-loss rates would still provide peak uplift rates of $\sim 0.75-1.10 \text{ mm/yr}$.

Figure 5. Testing the influence of plate boundary geometry on uplift variability. (a) Vertical rates inverted from the LOS maps in Figure 3. Peak vertical rates of $\sim 12 \text{ mm/yr}$ are found just north-east of Aoraki/Mt Cook (black diamond). The location of the vertical GNSS transect (Beavan et al., 2010) is marked as blue triangles, with squares showing the exhumation rates from a thermo-seismic exhumation model (Michailos et al., 2020). Vertical uplift rates have been filtered with a 2 km boxcar filter for clarity and contoured. Original results are shown in Figure S2 of Supporting Information S1. (b) 1% of the accepted geometries of the post-converged models following inversion of the InSAR velocities. Darker reds and blues indicate are increasingly likely locations for the Alpine Fault and mantle shear zone respectively, with black lines showing the optimal solution. The best-fitting dip of the slipping portion of the Alpine Fault indicated by the green line of the dip indicator. Full model breakdown and results in Figure 6i. (c) Three-component velocities for each profile, from InSAR inversion, 1% of accepted models, and the optimal model. GNSS velocities from (Beavan et al., 2010, 2016).

Viscoelastic modeling also shows localized variations in the uplift rate, although the magnitude of this impact varies based on the thickness of the elastic lid (Liu et al., 2024). A 15 km lid may produce up to 1 mm/yr of uplift at Aoraki/Mt Cook, although the relatively short time period over which this melting has occurred may favor a 50 km lid, resulting in a mostly negligible GIA rate, with some areas of ~ 0.3 mm/yr, although this also used the lower, pre-2000 deglaciation rate.

Although the upper bound of these estimates are potentially detectable in InSAR, in this case they occur close to glaciers in areas where InSAR coherence is already low (resulting in a relative lack of data, Figure 3) and noise levels therefore higher, as well as being highly sensitive to variables such as the accuracy of the estimates of spatial distribution of ice loss thicknesses and the chosen elastic thickness of the crust. Therefore, beyond showing the contribution is small, we do not consider the impact of deglaciation further, considering it an epistemic uncertainty for consideration in future study.

6. Structural Control on Spatial Variation in Interseismic Uplift

Our data shows a clear along-strike variability in Southern Alps uplift rates. Although numerical modeling has indicated that climate has a strong control on mean topographic and uplift asymmetry of the Southern Alps (Whipple, 2009), it is not clear that this should have an effect along strike. To assess the causes of this variability, we will invert our three-component velocity fields along three fault perpendicular profiles to distinguish between two possible end-members: (a) “tectonic aneurysm” caused by coupled surface and tectonic process resulting in localized elevated exhumation rates (Zeitler et al., 2014), or (b) uplift that is controlled by variations in the underlying structure of the Alpine Fault (Figure 5b).

Profiles are 50 km wide, and extend from 20 km NW of the fault (Australian Plate) to 100 km SE of the fault (Pacific Plate), meaning that the uplift velocities that required the most correction are not included in the inversion, although they have pinned the far-field to realistic values. We use a nested, rather than quad-tree sub-sampling method for the profiled data, where the profile is split into bins of -20–0, 0–20, 20–40, 40–60, and 60–100 km from the fault, and randomly sample 20%, 100%, 50%, 33%, and 25% of the available data, to result in an inversion that preferentially fits to the rapidly uplifting, near-field Pacific crust. Variance-covariance matrices are then made using semi-variograms from the same non-deforming region in the far field for each of the three inverted velocities (Figure S5 in Supporting Information S1) to account for spatially correlated noise.

We follow a proposed general structure beneath the Southern Alps where long-wavelength plate motion is partitioned into Pacific Plate convergence and a vertical strike-slip mantle shear zone, overlain by an inclined Alpine Fault capable of oblique fault-slip (Beavan et al., 2010; Norris & Toy, 2014; Stern et al., 2007). The model set-up is based on the deep structure of the Southern Alps laid out by Norris and Toy (2014), of three shear zones connected at a single point. Other models of the Alpine Fault allow for slip to be partitioned onto two separate crustal structures, with an inclined dip-slip plane truncating a sub-vertical strike-slip plane (e.g., Koons et al., 2003; Warren-Smith et al., 2022). There are additional faults in the Southern Alps, particularly those in the Otago region, that dip toward the Southern Alps and may be able to localize some deformation. Reported slip rates on such faults, however, are sufficiently low that any contribution to the present day vertical deformation will likely be within the noise levels of the InSAR (Beaumont et al., 1996; Seebeck et al., 2024).

We apply the modeling step to invert for the fault parameters based on the InSAR data using the Geodetic Bayesian Inversion Software (GBIS; Bagnardi & Hooper, 2018), allowing for variations in Alpine Fault geometry and slip-rates (Figures 5b and 6i). The Alpine Fault is represented as a dipping Okada dislocation (Okada, 1985) to allow for along-strike, local variations in horizontal and uplift deformation. Plate convergence is accommodated as dip-slip motion on a horizontal Okada dislocation beneath the Southern Alps, the leading edge of which is attached to the base of the Alpine Fault. To account for edge effects and potential uplift contributions from adjacent fault sections, the dislocations used are “pseudo-infinite.” We make no claims as to whether the horizontal shear represents a lower crustal decollement or not—rather it is there simply to represent the convergent component of plate motion, and as such shall be referred to as the convergent surface. The third shear zone is represented in the model as a vertical arctan screw dislocation beneath an elastic lid, held to be lower than the base of the Alpine Fault, with a rigidity contrast leading to asymmetrical surface velocities (Jolivet et al., 2008; Savage & Burford, 1973). This allows us to capture the long-wavelength fault parallel velocity variations across the plate margin (Figure 6b). All the dislocations are pseudo-infinite length, and the convergent surface is additionally

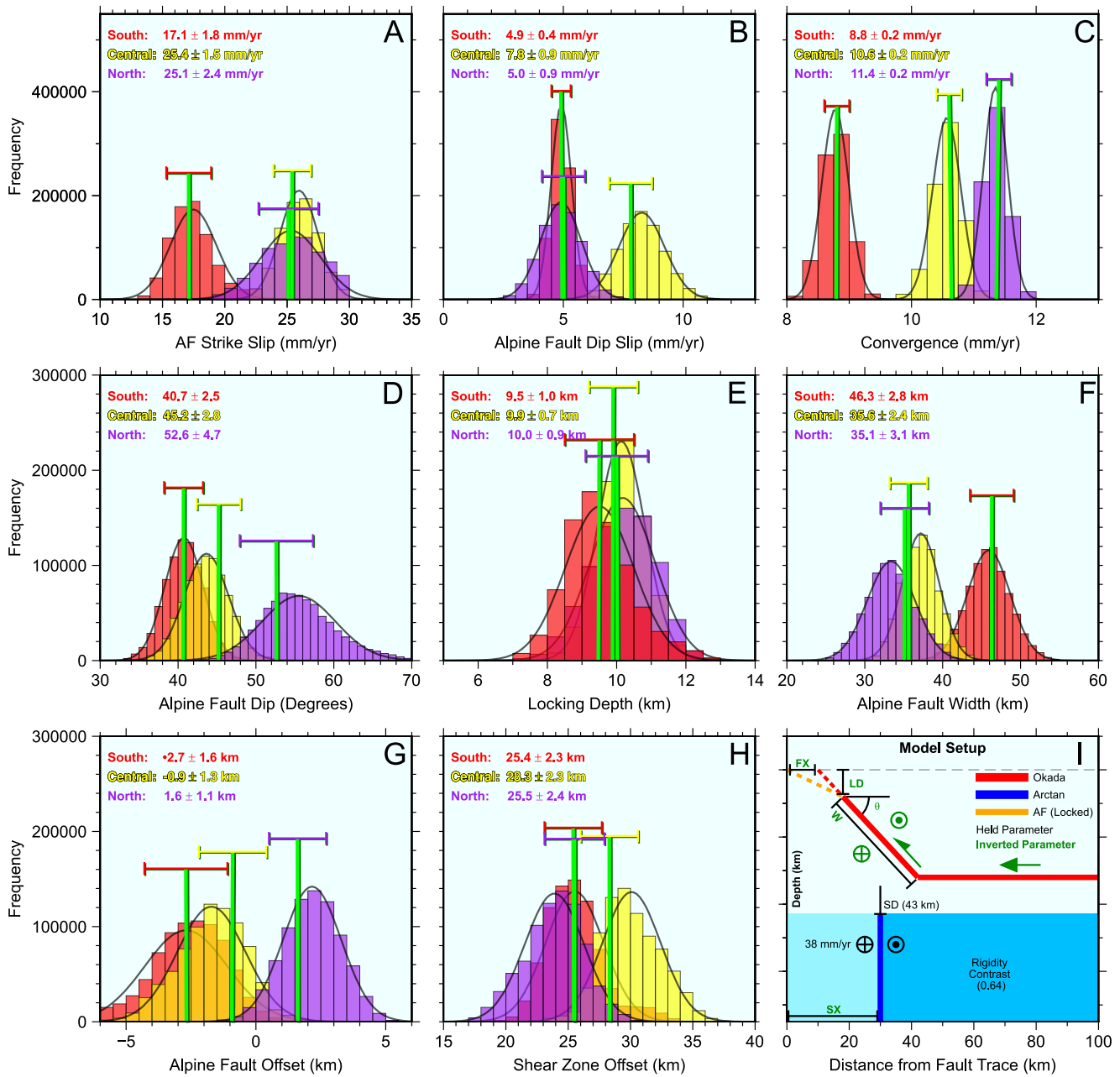


Figure 6. (a–h), Histograms of accepted post-burn-in model parameters. Green lines show the optimal value for each profile, and are differentiated by the color of the 1σ error bar at the top. (i) Schematic of the model setup, with held (black) and free (green) fault parameters. FX: Fault X-offset, LD: Locking Depth, W: Width of slipping portion of AF, SD: Shear zone locking Depth, SX: Shear zone X-offset, θ : Dip of slipping portion of the AF. Convergence (full green arrow) modeled as dip-slip on a horizontal Okada dislocation.

given pseudo-infinite width. The Alpine Fault is the only surface permitted both strike- and dip-slip. The convergent surface is provided only dip-slip, and the arctan vertical shear zone only strike-slip motion.

Additional Alpine Fault parameters that are inverted for are the locking depth, dip, width and an additional horizontal offset from the fault trace to allow for a difference in dip of the locked and slipping portions of the fault. For all permutations of Alpine Fault geometry, parameters of the convergent surface are recalculated so it is connected to the base of the Alpine Fault.

We look to have a uniform vertical shear zone beneath the three profiles, allowing us to consider variations between profiles as due to changes in the Alpine Fault. The shear zone is modeled as a strike-slip interface beneath the Alpine Fault, slipping at the plate motion-vector of 38 mm/yr, with a rigidity contrast allowing for asymmetric deformation, where 0.5 is no contrast, and 1 is all deformation occurring on the Pacific Plate (Jolivet et al., 2008). To assign a top depth and rigidity contrast, we invert the horizontal components of all InSAR and GNSS data within the study area, resulting in a top depth of 43 km and a rigidity contrast of 0.64 (Figure 6i). We allow variation in the horizontal offset of the shear zone between profiles. Consequently, the center of the characteristic arctan displacement profile is displaced from the fault trace, instead matching the shear zone location (Figure 5b).

We use a single screw dislocation rather than a distributed shear zone as the surface expression of distributed shear and a single dislocation is indistinguishable when the width of the shear zone is less than $\pi \times$ locking depth (Jolivet et al., 2008). At 35–45 km, this would therefore correlate to a zone 110–140 km wide. In addition to being potentially larger than the profiles themselves, this is also larger than the 100 km limit placed on a deforming mantle zone by Ellis, Beavan, and Eberhart-Phillips (2006). However, the location of a single dislocation would still represent the center of a distributed shear zone. We deem the use of elastic dislocations in our model as a valid simplifying assumption given that as the Alpine Fault is in the late stages of its seismic cycle, any viscous postseismic effects from the last great earthquake should not be detectable (Ellis, Beavan, Eberhart-Phillips, et al., 2006).

One million models were run through GBIS, with the first 20% discarded as burn-in (though convergence typically occurs within 10,000 runs), with the remaining 80% kept for analysis (Figure 6). Of the non-discarded models, we randomly select 1% (8,000) for display. Joint probabilities for each profile are shown in Figures S7–S9 of Supporting Information S1.

We resolve little along-strike variation in the shallow locked section of the Alpine Fault, with a consistent dip of $\sim 48^\circ \pm 7$ (similar to mapped surface trace values Barth et al., 2013) and 10 ± 1.5 km locking depth (Figure 7a), with the Alpine Fault extending to a depth of 35–40 km along across all three profiles (Figures 6 and 7b), as inferred from seismic reflection data (Stern et al., 2007). The slip-rates and fault parameters found in the southern profile are similar to that found by Liu et al. (2024), who also relied on Okada dislocations to model GNSS data. The main along-strike variations are the slip-rates and dip of the aseismically slipping deep Alpine Fault. From the north to south, the fault dip shallows from $53^\circ \pm 5$ to $41^\circ \pm 3$, with a decrease in a strike-slip rate from 24 to 25 mm/yr in the north and center to 17 mm/yr in the south. The decrease in the southern strike-slip component is only observed in other studies significantly further south (Wallace et al., 2007). There are several potential causes for this: an unexpectedly shallow locking depth resulting in a reduction of the required mean slip on the Alpine Fault (Figure 7 and Figure S7 in Supporting Information S1), no data from >100 km SE of the fault included in the inversion causing lack of some far-field deformation, and a potential influence of otherwise minor faults to the SE of the Alpine Fault (Litchfield et al., 2014; Seebeck et al., 2024).

Peak dip-slip rates of 8 ± 1 mm/yr in the central profile (encompasses the area of peak uplift) are an increase of $>50\%$ on the ~ 5 mm/yr rates to the north and south. This may be a lower limit on the peak dip-slip rate, however, as the profile width encompasses the entire uplift region (Figure 6). The inverted slip-rate must therefore be value that best fits the average slip from the central peak to the lower values along strike. The additional 3–6 mm/yr difference between the modeled and measured peak uplift rates are therefore likely a collection of (a) regions of higher slip at lower resolution than was modeled, (b) localized sources of uplift and (c) inherent noise within the data.

Our models show that there is a 13° shallowing of the Alpine fault from the northern to southern sections. Although seemingly abrupt, it is not unique on the Alpine Fault, with a 40° steepening of the fault at depth is observed from microseismicity at the transition from the Central Alpine Fault to the South Westland section at the Martyr River (Warren-Smith et al., 2022). It is unclear though as to whether the Martyr Transition is continuous over 5 km, or whether it represents a northern thrust sheet truncating a southern sub-vertical fault. It is therefore not beyond reason that the 13° shallowing could occur over a similarly short distance. As our model setup only permits a single fault of fixed strike, then the intermediate dip of the central profile may represent the optimal solution to accommodate the fault curve (Figure 7b). Variations in tectonic fabrics within exhumed rocks and the apparent thickness of metamorphic textural zones further indicate that this shallowing may occur over short length-scales (Little et al. (2005), Figure S3 in Supporting Information S1). The resulting increase in dip-slip rates in this region would therefore be a result of the formation of a fault-ramp oriented orthogonally to the plate motion

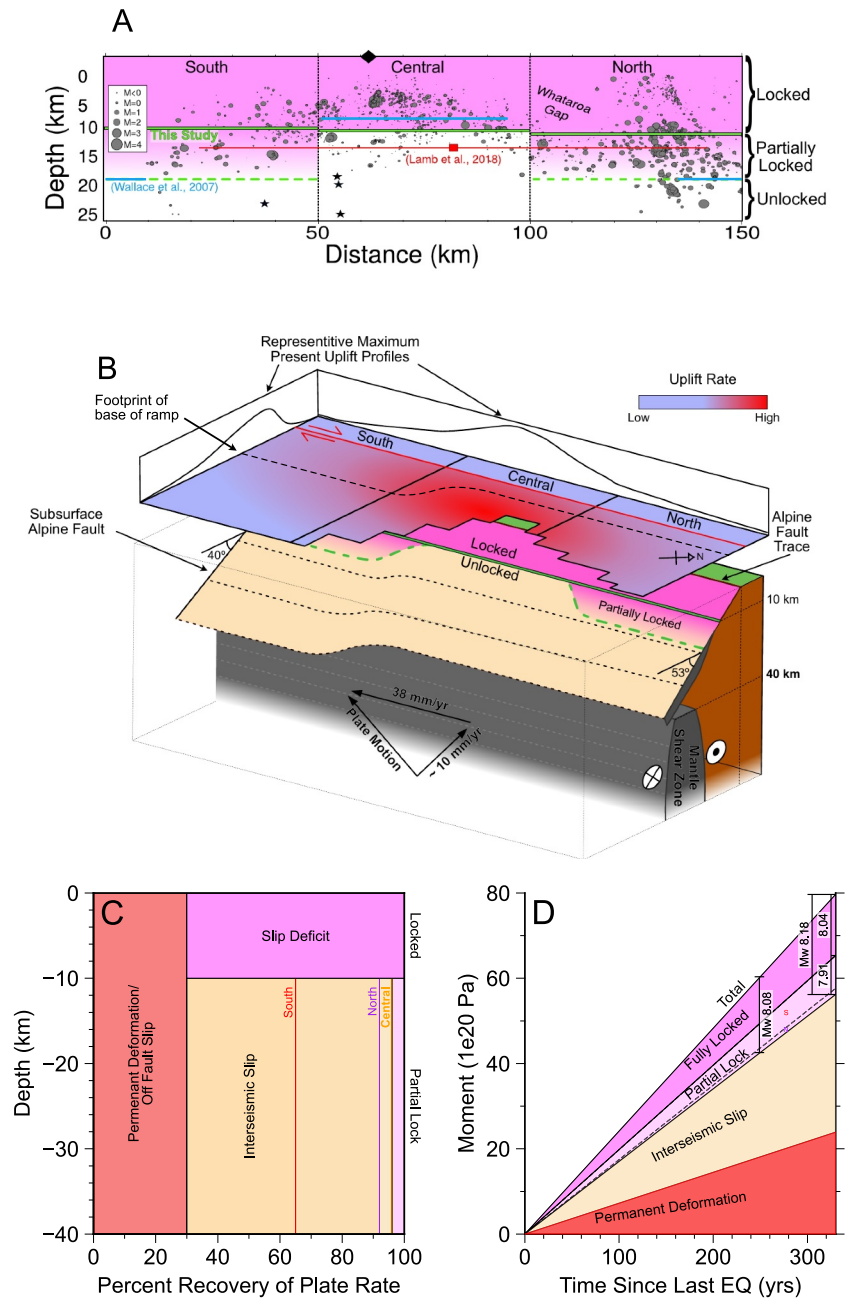


Figure 7. Inferred fault structure and slip-rate deficit for estimating coseismic contribution. (a) Locking lines of this study (green) and Lamb et al. (2018) (red), with 75% coupling line of Wallace et al. (2007) (blue). Instead of a constant locking depth, we expect a zone of partial locking extending from our reported depth to the base of seismicity (Michailos et al., 2019), equivalent to the $\sim 550^{\circ}\text{C}$ contour. (b) Schematic model of the Alpine Fault with approximate interseismic uplift location overlying the fault ramp. Modeled planar slip surfaces and dislocations are representative of broader shear zones (gray areas). Beige shows interseismically slipping sections of the Alpine Fault, and purple locked sections. The Alpine Fault ultimately steepens again to a vertical strike-slip fault SW of 169° , however this transition is beyond the scope of this study. (c) Simplified model of slip allocation as produced by the inversions, with 30% plate-motion accommodated by internal deformation and slip on minor faults (red). Vertical lines indicate the variable percentage of plate-motion accommodated by slip at depth for each profile. (d) Simplified budget of seismic moment over an earthquake cycle, following the color scheme of (c). The majority of coseismic moment comes from the slip on the shallow locked section, with a significant portion also due to the relatively low interseismic slip rate of the southern profile (c). The moment releases for 249 and 329 years recurrence intervals are shown (Howarth et al., 2021).

vector, causing the apparent locus of uplift due to more efficient transport of material up-fault due to an increase in the local fault-perpendicular rate at depth. An alternate mechanism for the locus of uplift would be due to the tectonic aneurysm effect, whereby focused erosion or glacial unloading results in an isostatic response, creating a feedback loop as the crust weakens due to local deflection of the thermal contours. This would be compatible with the peak uplift being associated with the location of an increased geotherm and thinning of the seismogenic thickness that would be expected following the rapid advection of lower crustal material (Figures 7a and Michailos et al., 2019). This would allow the uplift to occur without the need for geometric complexity on the fault, appearing as an increase in dip-slip rate without along-strike dip variation. It could not explain, however, the variation in thickness of the textural layering. Between the two models we set out to test, we therefore favor a structural control on the uplift distribution resulting from the restraining bend caused by the sharp change in dip as being the dominant control on the uplift distribution. As our model still slightly underestimates the uplift distribution in some regions, this allows for the possibility of additional contributions from other unmodelled sources such as unloading.

To see the correlation between current uplift and exhumation, we compare our results with the easily reproducible data from the exhumation rate models of Michailos et al. (2020), who use a mixture of short-term (regional catalogs of microseismicity) and long-term (thermochronological data) in their inversion. Like in this study, Michailos et al. (2020) consider the Southern Alps to be within a topographic steady state, providing a more suitable comparison of the modeling approaches. However, other earlier exhumation estimates exist for the area included in the review compilation by (Jiao et al., 2017). There is consistency between the locus of uplift, modeled locus of exhumation, and the change in surface thickness of mapped metamorphic textural zones expected from a 15° shallowing of the Alpine Fault (Figure 5a and Figure S3 in Supporting Information S1). This stability indicates a structural control that may prevent the migration of uplift along strike.

A structural control will prevent migration of the locus of uplift and exhumation. This stability is reflected in the similarity in locations of our locus of uplift, a modeled locus of exhumation, and the change in surface thickness of mapped metamorphic textural zones expected from a 15° shallowing of the Alpine Fault (Figure S3 in Supporting Information S1, Little et al., 2005; Michailos et al., 2020). An alternative structural control has been proposed on the focusing of uplift due to inherited characteristics of the crust. The Pacific Plate is generally thinner and stronger in the north Canterbury region than it is in the south. The thickening of the crust allows the Southern Alps deformation to be distributed over a larger area, whilst the thinner crust acts as an indenter to form localized uplift of the thicker crust in the central Southern Alps (Beaumont et al., 1996; Upton et al., 2009).

7. Accounting for Temporal Variability

Once the rates and causes of interseismic uplift are established, it is necessary to constrain the coseismic behavior of faulting in order to determine the short and long-term nature of uplift in this region. Variations in earthquake magnitude and recurrence time introduce uncertainty into estimations of coseismic displacement based on absolute slip deficit. However, by instead working in terms of slip-rate deficit rather than absolute slip, these issues can be circumvented, resulting in a model that is independent of the time since the last earthquake, requiring just the interseismic and long term slip-rates.

Overall, the strike-slip rate must equal the 38 mm/yr Pacific Plate rate. As the geologically derived slip rate on the Alpine Fault is 27 mm/yr, 30% of the Pacific Plate rate is recovered through distributed deformation of the Southern Alps rather than slip on the Alpine Fault (Figure 7c and Norris & Cooper, 2001). The remaining 70% is distributed across the Alpine Fault, to be recovered either by interseismic slip, or slip following an earthquake. As the Alpine Fault is toward the end of its seismic cycle (Berryman et al., 2012; Howarth et al., 2021), we can assume that the faults have returned to their interseismic rates, and that the inverted interseismic slip-rates do not contain any signals from postseismic slip (Ellis, Beavan, Eberhart-Phillips, et al., 2006). Over the course of a seismic cycle, below the 10 km locking depth over 90% of the plate rate is recovered in the northern and central profiles, and 65% in the south. The remaining plate rate, equal to 27 mm/yr on the locked portion of the fault, and ~4–13 mm/yr below 10 km, must be accommodated through earthquake induced slip. As the central Alpine Fault is one of the most periodic fault segments ever recorded (Berryman et al., 2012; Howarth et al., 2021), and there are good constraints on the seismic potential of the fault (Sutherland et al., 2007), we may be able to cross-check the coseismic moment release expected by this model against what is geologically plausible on this fault.

We estimate the moment release of future earthquakes as:

$$M_0 = M_0^{AF_{Lock}} + M_0^{AF_{Slip}} \quad (4)$$

where

$$M_0^{AF_{Lock}} = \mu \times L \times \frac{Z}{\sin(dip_{lock})} \times R_{geologic} \times T_{int} \quad (5)$$

and

$$M_0^{AF_{Slip}} = \mu \times L \times W \times (R_{geologic} - R_{AF_{Slip}}) \times T_{int} \quad (6)$$

where μ is the shear modulus, L is the length of fault to rupture (given as 380 km, Howarth et al., 2021), Z is the depth to the top of the slipping portion of the Alpine Fault, dip_{lock} is the dip of the surface trace of the Alpine Fault, $R_{geologic}$ is the geologic slip rate of the Alpine Fault (70% of the total plate motion vector (27 mm/yr, Norris & Cooper, 2001), W is the width of the fault, $R_{AF_{Slip}}$ is the magnitude of slip of the slipping portion of the Alpine Fault, and T_{int} is the length of time of the seismic cycle of the Alpine Fault (268–330 years (Berryman et al., 2012; Howarth et al., 2021)). Our model provides single values for each of these rates, which represent the average uniform slip over each fault section—a simplification of the heterogeneous slip distributions to be expected in reality.

For a M_w 8 earthquake, 380 km of the Alpine Fault can be expected to rupture (Howarth et al., 2021). As this is significantly longer than the 150 km of fault that formed part of this study, we extend our northern and southern faults to reach the total 380 km length, acknowledging that this is a first-order sanity check, and that in reality the fault properties cannot be expected to stay constant for so far. The total slip for the locked fault is the combined slip from the strike-slip component ($R_{geologic}$) and the dip-slip (set to equal the dip-slip accommodated on the deep Alpine Fault).

Our results show coseismic slip on the modeled locked portion of the faults would result in an earthquake in the range of M_w 7.9–8.0 (Figure 7c). Whilst slightly smaller than some of the largest ($M_w > 8$) earthquakes estimated to have occurred on the Alpine Fault, this is still within the range of large–great earthquakes deemed possible for the Alpine Fault (Howarth et al., 2021; Sutherland et al., 2007). This lower estimate is likely due to how locking is calculated in our approach. In our uniform slip model, surfaces can be considered either locked or unlocked, with the unlocked portion being where slip occurs (Figure 7b). Our estimation of locking depth is shallower (Figure 7a) than those from regional GNSS studies (12 km, Lamb et al., 2018), elastic block modeling (70% locked between 8 and 18 km, Wallace et al., 2007) and seismogenic depth (8–25 km, Michailos et al., 2019). We expect in reality a zone of partial coupling between our reported locking line and the base of seismicity, reflecting the deficit between our reported strike-slip rates on the deep portion of the fault and the long-term plate rate (Figure 7c). This would allow a contribution of coseismic moment from deep slip as well.

The relatively low amount of interseismic slip in the southern profile (matching increased coupling beneath 43.5°S from block modeling (Wallace et al., 2007)) means that the majority of the seismic moment from the partially locked region of the fault comes from the southern fault sections, with this contribution equivalent to M_w 7.8–7.9. This increases the total expected magnitude to M_w 8.1–8.2 (Figure 7d). It is unclear though how this additional moment is distributed across the deep fault. Our models require uniform slip across the whole deep fault. However, it is more likely that the locking percentage decreases from 100% at our reported locking line, to 0% near the base of seismicity, resulting in a locking profile more similar to that derived from elastic block modeling (Figure 7). This also does not consider any viscous responses to earthquakes such as deep postseismic slip or strain accommodation through distributed deformation, so it is likely that a substantial portion of the slip deficit on the deeper portions of the fault may be recovered postseismically, meaning that M_w 8.1–8.2 represents an upper-bound estimate of potential earthquake magnitude. There is ambiguity as to how the deep slip deficit is partitioned both along the fault, and between co- and post-seismic deformation. Therefore, we use only displacements from the modeled locked portion of the Alpine Fault. We consider this a lower bound on seismic potential, as the variation in the locking depth is certainly more complex than a singular 10 km locking line.

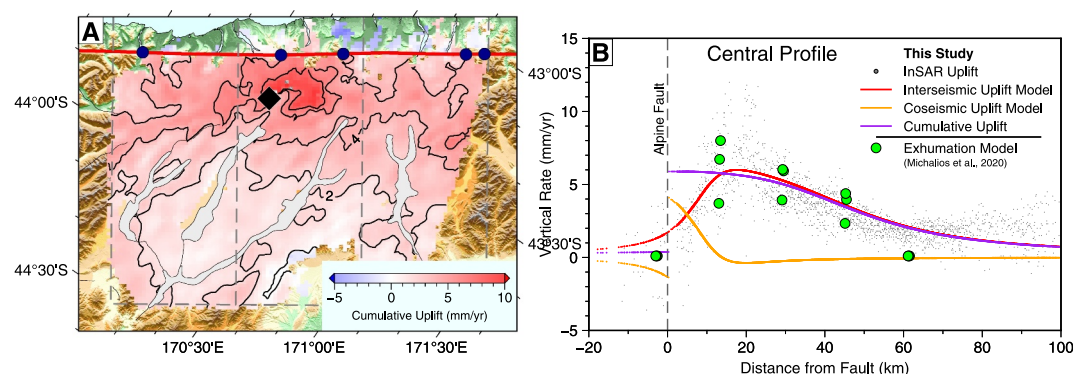


Figure 8. Model of the long-term exhumation of the central Southern Alps. (a) Spatial distribution of uplift (and therefore exhumation) taken by adding the modeled coseismic displacements directly to the inverted uplift rates (Figure 5a), allowing for higher rates close to the Alpine Fault than is resolved using the interseismic uplift model. Blue dots refer to the fault dip-slip measurements plotted in Figure 5a. (b) The total uplift rate over a seismic cycle (purple line) can be calculated by summing the interseismic uplift (InSAR pixel data, gray dots, or modeled interseismic uplift for the central profile, red line) with the modeled coseismic uplift (yellow line). Including the coseismic allows for uplift (and exhumation) to occur at the fault. Exhumation nodes from Michailos et al. (2020) are plotted for comparison. The similarity between cumulative uplift and exhumation nodes can support evidence of long-term stability that would allow cumulative uplift to be used as an exhumation proxy.

Furthermore, by excluding post-seismic slip, we potentially remove the ability of the fault system to recover any of the elastic component of the interseismic deformation.

These lower-bound earthquakes can contribute ~ 4 mm/yr of uplift at the fault trace. When added to the interseismic uplift rates, this allows peak cumulative uplift rates at the fault of 6–8 mm/yr, while far-field subsidence reduces peak uplift rates found between 15 and 35 km from the fault by < 1 mm/yr (Figure 8).

8. Spatially Resolved Short-Term Uplift as a Proxy for Exhumation

We applied our modeled coseismic displacements directly to our InSAR uplift maps to produce the spatial distribution of long-term bulk uplift rate. This provides an opportunity to create a first-order proxy for the long-term exhumation of the Southern Alps (Figure 8a). Applying the coseismic to the modeled interseismic is an option in the event of particularly noisy InSAR data, but the spatial resolution of the exhumation will be constrained to the profile widths, as well as likely underestimating the peak exhumation rates (Figure 8b). There remains a small underestimate of the bulk uplift rates compared to the geological dip-slip rates (Figure 5a), indicating that this coseismic model is only a lower bound. Steepening the dips of each fault segment to the 2σ values ($+5^\circ$) could increase the surface uplift rate by up to ~ 0.5 mm/yr. However, this is more likely explained by the imposition of additional local processes that have not been included in this model, such as intense erosional processes such as landsliding, glacial and fluvial erosion (Jiao et al., 2017; Liu et al., 2024; Roda-Boluda et al., 2023), small-scale segmentation of the Alpine Fault at the surface (Norris & Cooper, 1995), or the effect of topography on elastic inversion (Langer et al., 2019).

It is worth restating these caveats in order to consider the wider applicability of this approach to other orogenies. Primarily, the long term surface uplift rate must remain zero, with rock uplift offset by erosion and the resulting sediment removed. It is possible to grow relief whilst maintaining a constant mean surface, so we assume a constant maximum topography envelope as the slopes of individual peaks become oversteepened and therefore susceptible to landsliding. Consequently, because of our stated caveats in this scenario, we have been able to disregard that of isostatic adjustment, which otherwise can largely compensate erosion and uplift (Figures 1a and Molnar, 2012). Secondly, although a mean topographic surface is preserved, the along-strike location of peak uplift may be transient, resulting in a spatial offset between contemporary uplift and recorded exhumation. We show that this is unlikely in the Southern Alps by inverting for fault structure, with current uplift matching the recorded exhumation (Adams, 1980; Little et al., 2005; Michailos et al., 2020). Finally, there must be good constraints on the geological slip rates along major fault structures in order to identify the slip-rate deficits

required for coseismic modeling. Given these considerations, long-term rock uplift may be used as a proxy for the exhumation, allowing variations in its spatial distribution to be revealed.

Our method uses short-term measurements to place constraints on the long-term evolution of orogenies. Although we validate our approach against many studies carried out in the Southern Alps, not all of these are necessary to apply this method elsewhere. InSAR bulk uplift may be used as the proxy on the assumption that rock uplift is constant over multiple cycles if surface stability is previously established. However this assumption should not be made without reference to any other available data, as uplift rates can vary. If erosion or exhumation data are available, then it may also be possible to use InSAR data to establish that the system is under surface stability, through mass balance calculations, where InSAR derived fault structures and slip rates determine if the volume of added material maintains crustal thickness (Figure 1a), or through weight of evidence that uplift and erosion/exhumation are equal (e.g., Figure 1b).

9. Conclusion

We have generated a three-component velocity field over the Southern Alps of New Zealand, a rapidly deforming orogenic region, by utilizing data from multiple viewing SAR geometries from the past decade despite it proving a challenging target for current InSAR observations. This dense surface velocity map allows us to highlight both the across- and along-strike variations in uplift over an active orogeny, with peak uplift of ~ 1 cm/yr occurring in the Aoraki/Mt Cook region. We have provided geodetic evidence of a structural control on the locus of uplift, due to a 15° shallowing of the Alpine Fault, as suggested by some previous geological studies. Forward modeling of the slip-deficit on the interseismically locked region of the Alpine Fault shows that it is capable of hosting large-great earthquakes given the accumulated slip deficit. By considering both long-term uplift and the impacts of coseismic displacement we are able to generate a proxy for exhumation, showing that there is an important link between plate-boundary structure and the locus of exhumation, and have validated this result against other studies of exhumation. This indicates that although the impact of orographic precipitation has clear effects on orogenic evolution, the presence of a structural control may provide the initial impetus for the onset of uplift.

Conflict of Interest

The authors declare no conflicts of interest relevant to this study.

Data Availability Statement

Sentinel-1 SAR data is copyright of the European Space Agency, freely provided via the Alaska Satellite Facility (<https://asf.alaska.edu/>). Line-of-Sight and East-North-Up velocity fields are available in the supplementary materials, as is the final exhumation proxy. The GBIS version and inversion-ready data are additionally provided in supplementary materials. All data supplementary data and codes are additionally available at McGrath and Elliott (2025).

Acknowledgments

The authors would like to thank Shaozhuo Liu, Romain Jolivet, and other anonymous reviewers for insightful comments that improved the manuscript. Figures were made using the Generic Mapping Tools V6.2.0 (Wessel et al., 2019). Jack McGrath is supported through by a Natural Environment Research Council (NERC) studentship (NE/L002574/1) and GNS Science. This work is additionally supported by the UK NERC through Looking Inside Continents from Space (LiCS) at the Centre for the Observation and Modelling of Earthquakes, Volcanoes and Tectonics (COMET, <http://comet.nerc.ac.uk>). John Elliott gratefully acknowledges support from the Royal Society through a University Research Fellowship (UF150282 and URF/R/211006) and Research Grant (GF/R1/180076). This work was undertaken on ARC4, part of the High Performance Computing facilities at the University of Leeds, UK.

References

- Adams, J. (1980). Contemporary uplift and erosion of the Southern Alps, New Zealand. *GSA Bulletin*, 91(1), 1–114. <https://doi.org/10.1130/GSAB-P2-91-1>
- Adams, J. (1981). Uplift rates and thermal structure in the Alpine Fault zone and Alpine schists, Southern Alps, New Zealand. *Geological Society, London, Special Publications*, 9(1), 211–222. <https://doi.org/10.1144/gsl.sp.1981.009.01.19>
- Auriac, A., Sigmundsson, F., Hooper, A., Spaans, K. H., Björnsson, H., Pálsson, F., et al. (2014). InSAR observations and models of crustal deformation due to a glacial surge in Iceland. *Geophysical Journal International*, 198(3), 1329–1341. <https://doi.org/10.1093/gji/ggu205>
- Avouac, J. P. (2015). 6.09 - Mountain building: From earthquakes to geologic deformation. In G. Schubert (Ed.), *Treatise on geophysics* (2nd ed., pp. 381–432). Elsevier. <https://doi.org/10.1016/B978-0-444-53802-4.00120-2>
- Baden, C. W., Shuster, D. L., Aron, F., Fosdick, J. C., Bürgmann, R., & Hilley, G. E. (2022). Bridging earthquakes and mountain building in the Santa Cruz Mountains, CA. *Science Advances*, 8(8), eabi6031. <https://doi.org/10.1126/sciadv.abi6031>
- Bagnardi, M., & Hooper, A. (2018). Inversion of surface deformation data for rapid estimates of source parameters and uncertainties: A Bayesian approach. *Geochemistry, Geophysics, Geosystems*, 19(7), 2194–2211. <https://doi.org/10.1029/2018GC007585>
- Barth, N. C., Boulton, C., Carpenter, B. M., Batt, G. E., & Toy, V. G. (2013). Slip localization on the southern Alpine Fault, New Zealand. *Tectonics*, 32(3), 620–640. <https://doi.org/10.1002/tect.20041>
- Beaumont, C., Kamp, P. J. J., Hamilton, J., & Fullsack, P. (1996). The continental collision zone, South Island, New Zealand: Comparison of geodynamical models and observations. *Journal of Geophysical Research*, 101(B2), 3333–3359. <https://doi.org/10.1029/95jb02401>
- Beavan, J., Denys, P., Denham, M., Hager, B., Herring, T., & Molnar, P. (2010). Distribution of present-day vertical deformation across the Southern Alps, New Zealand, from 10 years of GPS data. *Geophysical Research Letters*, 37(16). <https://doi.org/10.1029/2010GL044165>

- Beavan, J., Tregoning, P., Bevis, M., Kato, T., & Meertens, C. (2002). Motion and rigidity of the Pacific Plate and implications for plate boundary deformation. *Journal of Geophysical Research*, 107(B10), ETG 19-1-ETG 19-15. <https://doi.org/10.1029/2001JB000282>
- Beavan, J., Wallace, L. M., Palmer, N., Denys, P., Ellis, S., Fournier, N., et al. (2016). New Zealand GPS velocity field: 1995–2013. *New Zealand Journal of Geology and Geophysics*, 59(1), 5–14. <https://doi.org/10.1080/00288306.2015.1112817>
- Bekaert, D. P. S., Walters, R. J., Wright, T. J., Hooper, A. J., & Parker, D. J. (2015). Statistical comparison of InSAR tropospheric correction techniques. *Remote Sensing of Environment*, 170, 40–47. <https://doi.org/10.1016/j.rse.2015.08.035>
- Berryman, K. R., Cochran, U. A., Clark, K. J., Biasi, G. P., Langridge, R. M., & Villamor, P. (2012). Major earthquakes occur regularly on an isolated plate boundary fault. *Science*, 336(6089), 1690–1693. <https://doi.org/10.1126/science.1218959>
- Biggs, J., Wright, T., Lu, Z., & Parsons, B. (2007). Multi-interferogram method for measuring interseismic deformation: Denali Fault, Alaska. *Geophysical Journal International*, 170(3), 1165–1179. <https://doi.org/10.1111/j.1365-246X.2007.03415.x>
- Biggs, J., & Wright, T. J. (2020). How satellite InSAR has grown from opportunistic science to routine monitoring over the last decade. *Nature Communications*, 11(1), 3863. <https://doi.org/10.1038/s41467-020-17587-6>
- Boussinesq, J. (1878). Équilibre d'élasticité d'un sol isotrope sans pesanteur, supportant différents poids. *CR Math. Acad. Sci. Paris*, 86(86), 1260–1263.
- Brouwer, W. S., & Hanssen, R. F. (2021). An analysis of InSAR Displacement vector decomposition fallacies and the strap-down solution. In 2021 IEEE International Geoscience and Remote Sensing Symposium IGARSS (pp. 2927–2930). <https://doi.org/10.1109/IGARSS47720.2021.9554216>
- Bull, W. B., & Cooper, A. F. (1986). Uplifted marine terraces along the alpine fault, New Zealand. *Science*, 234(4781), 1225–1228. <https://doi.org/10.1126/science.234.4781.1225>
- Carrivick, J. L., James, W. H. M., Grimes, M., Sutherland, J. L., & Lorrey, A. M. (2020). Ice thickness and volume changes across the Southern Alps, New Zealand, from the little ice age to present. *Scientific Reports*, 10(1), 13392. <https://doi.org/10.1038/s41598-020-70276-8>
- Crosetto, M., Solari, L., Mróz, M., Balasis-Levinsen, J., Casagli, N., Frei, M., et al. (2020). The evolution of wide-area DInSAR: From regional and national services to the European Ground Motion Service. *Remote Sensing*, 12(12), 2043. <https://doi.org/10.3390/rs12122043>
- Dal Zilio, L., Hetényi, G., Hubbard, J., & Bollinger, L. (2021). Building the Himalaya from tectonic to earthquake scales. *Nature Reviews Earth & Environment*, 2(4), 251–268. <https://doi.org/10.1038/s43017-021-00143-1>
- Elliott, J. R., Jolivet, R., Gonzalez, P. J., Avouac, J. P., Hollingsworth, J., Searle, M. P., & Stevens, V. L. (2016). Himalayan megathrust geometry and relation to topography revealed by the Gorkha earthquake. *Nature Geoscience*, 9(2), 174–180. <https://doi.org/10.1038/ngeo2623>
- Ellis, S., Beavan, J., & Eberhart-Phillips, D. (2006). Bounds on the width of mantle lithosphere flow derived from surface geodetic measurements: Application to the central Southern Alps, New Zealand. *Geophysical Journal International*, 166(1), 403–417. <https://doi.org/10.1111/j.1365-246X.2006.02918.x>
- Ellis, S., Beavan, J., Eberhart-Phillips, D., & Stöckhert, B. (2006). Simplified models of the Alpine Fault seismic cycle: Stress transfer in the mid-crust. *Geophysical Journal International*, 166(1), 386–402. <https://doi.org/10.1111/j.1365-246X.2006.02917.x>
- England, P., & Molnar, P. (1990). Surface uplift, uplift of rocks, and exhumation of rocks. *Geology*, 18(12), 1173–1177. [https://doi.org/10.1130/0091-7613\(1990\)018\(1173:SUORA\)2.3.CO;2](https://doi.org/10.1130/0091-7613(1990)018(1173:SUORA)2.3.CO;2)
- Francis, O. R., Hales, T. C., Hobley, D. E. J., Fan, X., Horton, A. J., Scaringi, G., & Huang, R. (2020). The impact of earthquakes on orogen-scale exhumation. *Earth Surface Dynamics*, 8(3), 579–593. <https://doi.org/10.5194/esurf-8-579-2020>
- Haines, A. J., & Wallace, L. M. (2020). New Zealand-wide geodetic strain rates using a physics-based approach. *Geophysical Research Letters*, 47(1), e2019GL084606. <https://doi.org/10.1029/2019GL084606>
- Hamling, I. J., Wright, T. J., Hreinsdóttir, S., & Wallace, L. M. (2022). A snapshot of New Zealand's dynamic deformation field from Envisat InSAR and GNSS observations between 2003 and 2011. *Geophysical Research Letters*, 49(2), e2021GL096465. <https://doi.org/10.1029/2021GL096465>
- Han, X., Dai, J.-G., Smith, A. G. G., Xu, S.-Y., Liu, B.-R., Wang, C.-S., & Fox, M. (2024). Recent uplift of Chomolungma enhanced by river drainage piracy. *Nature Geoscience*, 17(10), 1031–1037. <https://doi.org/10.1038/s41561-024-01535-w>
- Herman, F., Cox, S. C., & Kamp, P. J. J. (2009). Low-temperature thermochronology and thermokinematic modeling of deformation, exhumation, and development of topography in the central Southern Alps, New Zealand. *Tectonics*, 28(5). <https://doi.org/10.1029/2008TC002367>
- Herman, F., Rhodes, E. J., Braun, J., & Heiniger, L. (2010). Uniform erosion rates and relief amplitude during glacial cycles in the Southern Alps of New Zealand, as revealed from OSL-thermochronology. *Earth and Planetary Science Letters*, 297(1), 183–189. <https://doi.org/10.1016/j.epsl.2010.06.019>
- Hilton, R. G., & West, A. J. (2020). Mountains, erosion and the carbon cycle. *Nature Reviews Earth & Environment*, 1(6), 284–299. <https://doi.org/10.1038/s43017-020-0058-6>
- Hooper, A., Bekaert, D., Spaans, K., & Ar, M. (2012). Recent advances in SAR interferometry time series analysis for measuring crustal deformation. *Tectonophysics*, 13.
- Houlié, N., & Stern, T. (2017). Vertical tectonics at an active continental margin. *Earth and Planetary Science Letters*, 457, 292–301. <https://doi.org/10.1016/j.epsl.2016.10.018>
- Hovius, N., Stark, C. P., & Allen, P. A. (1997). Sediment flux from a mountain belt derived by landslide mapping. *Geology*, 25(3), 231. [https://doi.org/10.1130/0091-7613\(1997\)025\(0231:SFFAMB\)2.3.CO;2](https://doi.org/10.1130/0091-7613(1997)025(0231:SFFAMB)2.3.CO;2)
- Howarth, J. D., Barth, N. C., Fitzsimons, S. J., Richards-Dinger, K., Clark, K. J., Biasi, G. P., et al. (2021). Spatiotemporal clustering of great earthquakes on a transform fault controlled by geometry. *Nature Geoscience*, 14(5), 314–320. <https://doi.org/10.1038/s41561-021-00721-4>
- Hubbard, J., Almeida, R., Foster, A., Sapkota, S. N., Bürgi, P., & Tapponnier, P. (2016). Structural segmentation controlled the 2015 Mw 7.8 Gorkha earthquake rupture in Nepal. *Geology*, 44(8), 639–642. <https://doi.org/10.1130/G38077.1>
- Hussain, E., Hooper, A., Wright, T. J., Walters, R. J., & Bekaert, D. P. S. (2016). Interseismic strain accumulation across the central North Anatolian Fault from iteratively unwrapped InSAR measurements. *Journal of Geophysical Research: Solid Earth*, 121(12), 9000–9019. <https://doi.org/10.1002/2016JB013108>
- Hussain, E., Wright, T. J., Walters, R. J., Bekaert, D., Hooper, A., & Houseman, G. A. (2016). Geodetic observations of postseismic creep in the decade after the 1999 Izmit earthquake, Turkey: Implications for a shallow slip deficit. *Journal of Geophysical Research: Solid Earth*, 121(4), 2980–3001. <https://doi.org/10.1002/2015JB012737>
- Jiao, R., Herman, F., & Seward, D. (2017). Late Cenozoic exhumation model of New Zealand: Impacts from tectonics and climate. *Earth-Science Reviews*, 166, 286–298. <https://doi.org/10.1016/j.earscirev.2017.01.003>
- Jolivet, R., Cattin, R., Chamot-Rooke, N., Lasserre, C., & Peltzer, G. (2008). Thin-plate modeling of interseismic deformation and asymmetry across the Altyn Tagh fault zone. *Geophysical Research Letters*, 35(2). <https://doi.org/10.1029/2007GL031511>
- Koons, P. O., Norris, R. J., Craw, D., & Cooper, A. F. (2003). Influence of exhumation on the structural evolution of transpressional plate boundaries: An example from the Southern Alps, New Zealand, 4.

- Kreemer, C., Blewitt, G., & Klein, E. C. (2014). A geodetic plate motion and Global Strain Rate Model. *Geochemistry, Geophysics, Geosystems*, 15(10), 3849–3889. <https://doi.org/10.1002/2014GC005407>
- Lamb, S., Arnold, R., & Moore, J. D. P. P. (2018). Locking on a megathrust as a cause of distributed faulting and fault-jumping earthquakes. *Nature Geoscience*, 11(11), 871–875. <https://doi.org/10.1038/s41561-018-0230-5>
- Langer, L., Gharti, H. N., & Tromp, J. (2019). Impact of topography and three-dimensional heterogeneity on coseismic deformation. *Geophysical Journal International*, 217(2), 866–878. <https://doi.org/10.1093/gji/ggz060>
- Langridge, R., Ries, W., Litchfield, N., Villamor, P., Van Dissen, R., Barrell, D., et al. (2016). The New Zealand active faults database. *New Zealand Journal of Geology and Geophysics*, 59(1), 86–96. <https://doi.org/10.1080/00288306.2015.1112818>
- Lazecký, M., Spaans, K., González, P. J., Maghsoudi, Y., Morishita, Y., Albino, F., et al. (2020). LiCSAR: An automatic InSAR tool for measuring and monitoring tectonic and volcanic activity. *Remote Sensing*, 12(15), 2430. <https://doi.org/10.3390/rs12152430>
- Li, G., West, A. J., & Qiu, H. (2019). Competing effects of Mountain uplift and landslide erosion over earthquake cycles. *Journal of Geophysical Research: Solid Earth*, 124(5), 5101–5133. <https://doi.org/10.1029/2018JB016986>
- Litchfield, N. J., Van Dissen, R., Sutherland, R., Barnes, P. M., Cox, S. C., Norris, R., et al. (2014). A model of active faulting in New Zealand. *New Zealand Journal of Geology and Geophysics*, 57(1), 32–56. <https://doi.org/10.1080/00288306.2013.854256>
- Little, T. A., Cox, S., Vry, J. K., & Batt, G. (2005). Variations in exhumation level and uplift rate along the oblique-slip Alpine Fault, central Southern Alps, New Zealand. *Bulletin of the Geological Society of America*, 117(5–6), 707–723. <https://doi.org/10.1130/B25500.1>
- Liu, S., Moulin, A., & Jónsson, S. (2024). Unloading uplift caused by surface processes in New Zealand's Southern Alps. *Geophysical Research Letters*, 51(15), e2024GL109019. <https://doi.org/10.1029/2024GL109019>
- McGrath, J., & Elliott, J. R. (2025). Linking geodetically resolved uplift to long-term orogenic exhumation in the Southern Alps, New Zealand [Dataset]. *Zenodo*. <https://doi.org/10.5281/zenodo.15541458>
- Michailos, K., Smith, E. G., Chamberlain, C. J., Savage, M. K., & Townend, J. (2019). Variations in seismogenic thickness along the central alpine fault, New Zealand, revealed by a decade's relocated microseismicity. *Geochemistry, Geophysics, Geosystems*, 20(1), 470–486. <https://doi.org/10.1029/2018GC007743>
- Michailos, K., Sutherland, R., Townend, J., & Savage, M. K. (2020). Crustal thermal structure and exhumation rates in the Southern Alps near the central alpine fault, New Zealand. *Geochemistry, Geophysics, Geosystems*, 21(8), e2020GC008972. <https://doi.org/10.1029/2020GC008972>
- Molnar, P. (2012). Isostasy can't be ignored. *Nature Geoscience*, 5(2), 83. <https://doi.org/10.1038/ngeo1383>
- Molnar, P., & England, P. (1990). Late Cenozoic uplift of mountain ranges and global climate change: Chicken or egg? *Nature*, 346(6279), 29–34. <https://doi.org/10.1038/346029a0>
- Morishita, Y., Lazecky, M., Wright, T. J., Weiss, J. R., Elliott, J. R., & Hooper, A. (2020). LiCSBAS: An open-source InSAR time series analysis package integrated with the LiCSAR automated Sentinel-1 InSAR processor. *Remote Sensing*, 12(3), 424. <https://doi.org/10.3390/rs12030424>
- Norris, R. J., & Cooper, A. F. (1995). Origin of small-scale segmentation and transpressional thrusting along the Alpine Fault, New Zealand. *Geological Society of America Bulletin*, 107(2), 231. [https://doi.org/10.1130/0016-7606\(1995\)107<0231:OOSSSA>2.3.CO;2](https://doi.org/10.1130/0016-7606(1995)107<0231:OOSSSA>2.3.CO;2)
- Norris, R. J., & Cooper, A. F. (2001). Late Quaternary slip rates and slip partitioning on the Alpine Fault, New Zealand. *Journal of Structural Geology*, 23(2–3), 507–520. [https://doi.org/10.1016/S0191-8141\(00\)00122-X](https://doi.org/10.1016/S0191-8141(00)00122-X)
- Norris, R. J., & Toy, V. G. (2014). Continental transforms: A view from the Alpine Fault. *Journal of Structural Geology*, 64, 3–31. <https://doi.org/10.1016/j.jsg.2014.03.003>
- Okada, Y. (1985). Surface deformation due to shear and tensile faults in a half-space. *Bulletin of the Seismological Society of America*, 75(4), 1135–1154. <https://doi.org/10.1785/BSSA0750041135>
- Parker, R. N., Densmore, A. L., Rosser, N. J., De Michele, M., Li, Y., Huang, R., et al. (2011). Mass wasting triggered by the 2008 Wenchuan earthquake is greater than orogenic growth. *Nature Geoscience*, 4(7), 449–452. <https://doi.org/10.1038/ngeo1154>
- Roda-Boluda, D. C., Schildgen, T. F., Wittmann, H., Tofelde, S., Bufer, A., Prancevic, J., & Hovius, N. (2023). Elevation-Dependent periglacial and paraglacial processes modulate tectonically-controlled erosion of the Western Southern Alps, New Zealand. *Journal of Geophysical Research: Earth Surface*, 128(11), e2023JF007271. <https://doi.org/10.1029/2023JF007271>
- Savage, J. C., & Burford, R. O. (1973). Geodetic determination of relative plate motion in central California. *Journal of Geophysical Research*, 78(5), 832–845. <https://doi.org/10.1029/JB078i005p00832>
- Schumacher, M., King, M. A., Rougier, J., Sha, Z., Khan, S. A., & Bamber, J. L. (2018). A new global GPS data set for testing and improving modelled GIA uplift rates. *Geophysical Journal International*, 214(3), 2164–2176. <https://doi.org/10.1093/gji/ggy235>
- Seebeck, H., Van Dissen, R., Litchfield, N., Barnes, P. M., Nicol, A., Langridge, R., et al. (2024). The New Zealand Community Fault Model – Version 1.0: An improved geological foundation for seismic hazard modelling. *New Zealand Journal of Geology and Geophysics*, 67(2), 209–229. <https://doi.org/10.1080/00288306.2023.2181362>
- Simpson, G. D. H., Cooper, A. F., & Norris, R. J. (1994). Late Quaternary evolution of the alpine fault Zone at Paringa, South Westland, New Zealand. *New Zealand Journal of Geology and Geophysics*, 37(1), 49–58. <https://doi.org/10.1080/00288306.1994.9514600>
- Stern, T., Okaya, D., Kleffmann, S., Scherwath, M., Henrys, S., & Davey, F. (2007). Geophysical exploration and dynamics of the alpine fault Zone. *Geophysical Monograph Series*, 175, 207–233. <https://doi.org/10.1029/175gm11>
- Stevens, V. L., & Avouac, J. P. (2015). Interseismic coupling on the main Himalayan thrust. *Geophysical Research Letters*, 42(14), 5828–5837. <https://doi.org/10.1002/2015GL064845>
- Sutherland, R. (1995). The Australia-Pacific boundary and Cenozoic plate motions in the SW Pacific: Some constraints from Geosat data. *Tectonics*, 14(4), 819–831. <https://doi.org/10.1029/95TC00930>
- Sutherland, R., Eberhart-Phillips, D., Harris, R. A., Stern, T., Beavan, J., Ellis, S., et al. (2007). Do great earthquakes occur on the Alpine Fault in central South Island, New Zealand? *Geophysical Monograph Series*, 175, 235–251. <https://doi.org/10.1029/175gm12>
- Tada, R., Zheng, H., & Clift, P. D. (2016). Evolution and variability of the Asian monsoon and its potential linkage with uplift of the Himalaya and Tibetan Plateau. *Progress in Earth and Planetary Science*, 3(1), 4. <https://doi.org/10.1186/s40645-016-0080-y>
- Tesauro, M., Kaban, M. K., & Cloetingh, S. A. (2013). Global model for the lithospheric strength and effective elastic thickness. *Tectonophysics*, 602, 78–86. <https://doi.org/10.1016/j.tecto.2013.01.006>
- Upton, P., Koons, P. O., Craw, D., Henderson, C. M., & Enlow, R. (2009). Along-strike differences in the Southern Alps of New Zealand: Consequences of inherited variation in rheology. *Tectonics*, 28(2). <https://doi.org/10.1029/2008TC002353>
- Wallace, L. M., Beavan, J., McCaffrey, R., Berryman, K., & Denys, P. (2007). Balancing the plate motion budget in the South Island, New Zealand using GPS, geological and seismological data. *Geophysical Journal International*, 168(1), 332–352. <https://doi.org/10.1111/j.1365-246X.2006.03183.x>
- Wang, K., Hu, Y., & He, J. (2012). Deformation cycles of subduction earthquakes in a viscoelastic Earth. *Nature*, 484(7394), 327–332. <https://doi.org/10.1038/nature11032>

- Warren-Smith, E., Townend, J., Chamberlain, C. J., Boulton, C., & Michailos, K. (2022). Heterogeneity in microseismicity and stress near rupture-limiting section boundaries along the late-interseismic alpine fault. *Journal of Geophysical Research: Solid Earth*, 127(10), e2022JB025219. <https://doi.org/10.1029/2022JB025219>
- Weiss, J. R., Qiu, Q., Barbot, S., Wright, T. J., Foster, J. H., Saunders, A., et al. (2019). Illuminating subduction zone rheological properties in the wake of a giant earthquake. *Science Advances*, 5(12), eaax6720. <https://doi.org/10.1126/sciadv.aax6720>
- Weiss, J. R., Walters, R. J., Morishita, Y., Wright, T. J., Lazecky, M., Wang, H., et al. (2020). High-Resolution surface velocities and strain for Anatolia from Sentinel-1 InSAR and GNSS data. *Geophysical Research Letters*, 47(17), e2020GL087376. <https://doi.org/10.1029/2020GL087376>
- Wessel, P., Luis, J. F., Uieda, L., Scharroo, R., Wobbe, F., Smith, W. H. F., & Tian, D. (2019). The generic mapping tools version 6. *Geochemistry, Geophysics, Geosystems*, 20(11), 5556–5564. <https://doi.org/10.1029/2019GC008515>
- Whipple, K. X. (2009). The influence of climate on the tectonic evolution of mountain belts. *Nature Geoscience*, 2(2), 97–104. <https://doi.org/10.1038/ngeo413>
- Willett, S. D. (1999). Orogeny and orography: The effects of erosion on the structure of mountain belts. *Journal of Geophysical Research*, 104(B12), 28957–28981. <https://doi.org/10.1029/1999JB900248>
- Willett, S. D., & Brandon, M. T. (2002). On steady states in mountain belts. *Geology*, 30(2), 175. [https://doi.org/10.1130/0091-7613\(2002\)030\(0175:OSSIMB\)2.0.CO;2](https://doi.org/10.1130/0091-7613(2002)030(0175:OSSIMB)2.0.CO;2)
- Wright, T., Houseman, G., Fang, J., Maghsoudi, Y., Hooper, A., Elliott, J., et al. (2023). High-resolution geodetic strain rate field reveals dynamics of the India-Eurasia collision (Preprint). *Physical Sciences and Mathematics*. <https://doi.org/10.31223/X5G95R>
- Wright, T., Parsons, B. E., & Lu, Z. (2004). Toward mapping surface deformation in three dimensions using InSAR. *Geophysical Research Letters*, 31(1). <https://doi.org/10.1029/2003GL018827>
- Zeitler, P. K., Meltzer, A. S., Brown, L., Kidd, W. S., Lim, C., & Enkelmann, E. (2014). Tectonics and topographic evolution of Namche Barwa and the easternmost Lhasa block, Tibet. In *Toward an improved understanding of uplift mechanisms and the elevation history of the Tibetan Plateau*. Geological Society of America. [https://doi.org/10.1130/2014.2507\(02\)](https://doi.org/10.1130/2014.2507(02))